Characterization of Non-Stationary Signals in Electric Grids: a Functional Dictionary Approach

Alexandra Karpilow, *Student Member, IEEE,* Asja Derviškadić, Guglielmo Frigo, *Member, IEEE,* and Mario Paolone, *Senior Member, IEEE*

***Abstract*—With the expanding role of converter-interfaced distributed energy resources, modern power grids are evolving towards low-inertia networks that are increasingly vulnerable to extreme dynamics. Consequently, advanced signal processing techniques are needed to accurately characterize measured signals in power systems during non-stationary conditions. However, as advocated by recent literature, state-of-the-art phasor estimation methods are unable to sufficiently capture the broadband nature of these signal dynamics since they rely on a quasi-steady state, single tone model. Inspired by previous work by the authors, this paper proposes a signal processing method that uses a dictionary of kernels, modeling common signal dynamics, to compress time-domain information into a few coefficients. The identified signal model and the extracted coefficients capture the broadband spectrum of typical power system signal dynamics and allow for an improved reconstruction of the measured signal.**

***Index Terms*—dictionary analysis, power system dynamics, phasors, transient analysis, compressed sensing**

I. Introduction

As we transition towards power grids based on distributed renewable energy and power converters, the inertial capacity of the grid is curtailed, increasing the likelihood of extreme dynamic behavior. Indeed, several real-world disturbances have been recorded recently with frequency ramps preceding blackouts like the one in Australia in 2016 [1], phase steps occurring during the faults in California in 2016 and 2017 [2], [3], or amplitude modulations as seen in the Continental European interconnected system in 2017 [4].

In this context, *Phasor Measurement Units* (PMUs) are viewed as a critical tool in the future of measurement, control and protections schemes in power grids [5]. With applications in state estimation, fault detection and location, security/protection and voltage stability analysis, PMUs have garnered significant attention in recent years. However, these measurement devices employ signal processing techniques based on steady state phasor models, the suitability of which is questionable in the presence of significant electromechanical transients. Phasor analysis relies on the extraction of a single fundamental tone that is assumed to be stationary for the duration of the observation window. However, as thoroughly explored in literature [6]–[9], signal dynamics (e.g., variations or steps in the amplitude or phase) have broadband frequency spectra that cannot be sufficiently approximated by narrow-band phasor models.

The characterization of signal dynamics in power grids is, therefore, an open question with a vast collection of related research. Many techniques attempt to improve estimations of an underlying phasor by approximating the dynamic component using Taylor series expansions or the *Taylor-Fourier* (TF) transform and Weighted Least Squares [10], [11]. In [11], when the extracted phasor model does not sufficiently match the true signal, the window length is reduced and the algorithm repeated in order to better satisfy the stationary assumption. Alternatively, *Compressed Sensing* (CS) techniques and the TF transform are used in [12] to identify the 1^{st} and 2^{nd} order derivatives of the phasor in order to account for variation in the corresponding signal model parameters. During slow dynamic operating conditions, dynamic phasor methods improve estimations of the static phasor parameters and the time-domain reconstruction. However, dynamic phasor models are unable to represent faster variations or discontinuities in the waveform which could lead to inaccurate frequency estimations, erroneous power flow calculations and inappropriate control actions [6], [7]. Furthermore, including the first and second order derivatives of the phasor in the time-domain reconstruction, according to the techniques presented in [11] and [12], requires large matrices of coefficients proportional in size to the length of the window and the Taylor expansion order. Other techniques offer improved signal models using O-splines or sinc interpolation in order to estimate oscillatory modes [13], [14] but are limited by the modulation model and may not be applicable for other common signal dynamics characterizing the behavior of low-inertia grids.

Instead, in this paper, we propose a technique to fully capture power system signal dynamics and provide essential information on the state of the grid. Building off of the study in [6], which applies the *Hilbert Transform* (HT) in the analysis of dynamic signals, we have developed the *Functional Basis Analysis* (FBA) algorithm for the identification and characterization of signal dynamics. The FBA method employs a dictionary with kernels generated using parameterised models of signal dynamics common in power grids. The dictionary is used to identify the kernel and its associated parameters that best match the given signal. For comparison, while the Fourier Transform relies on a basis of sinusoidal functions at discrete frequencies, the FBA dictionary is not restricted to

A. Karpilow and M. Paolone are with the École Polytechnique Fédérale de Lausanne (EPFL), CH-1015, Switzerland.
A. Derviškadić is with Swissgrid Ltd., Aarau, 5001, Switzerland.
G. Frigo is with the Swiss Federal Institute of Metrology (METAS), 3003 Bern-Wabern, Switzerland

This project is carried out within the frame of the Swiss Centre for Competence in Energy Research on the Future Swiss Electrical Infrastructure (SCCER-FURIES) with the financial support of the Swiss Innovation Agency (Innosuisse - SCCER program).

stationary sinusoids and is instead user-engineered to capture diverse signal dynamics. In this paper, we focus on the analysis and characterization of modulations and abrupt steps in the amplitude and phase of the signal as well as ramping of the instantaneous frequency. Depending on how the algorithm is designed, the FBA method could be extended to analyze higher frequency events, as demonstrated by the harmonic analysis example in Appendix C.

The paper is structured as follows: Section II explores the theory supporting the dictionary's design and modeling of common signal dynamics. Section III describes the proposed FBA algorithm including parameter extraction and identification of the signal dynamic. In Section IV, we demonstrate the performance of the algorithm when applied to synthetic signal dynamics or data from real grid events, and compare it with static and dynamic phasor estimation methods. Finally, in Section V, we conclude the paper by providing some remarks on the performance and potential of the algorithm in the processing of power grid dynamic signals.

II. Theory

The problem addressed in this paper is framed as follows: given a voltage or current signal from a power grid measurement device, identify the true underlying signal dynamic responsible for the corresponding continuous frequency spectrum and estimate the parameters that best characterize the signal. Because the set of possible signal dynamics that are likely to occur in power systems is finite, it can be sufficiently spanned by a dictionary of functions modeling various common signals (e.g., phase modulations, frequency ramps) [6]. In the proposed FBA algorithm, the dictionary is composed of parameterized kernels that represent the frequency spectrum of known signal dynamics. The FBA algorithm leverages properties of analytic signals in the creation of dictionary kernels in order to eliminate long-range spectral leakage caused by the negative spectrum. For this reason, we recall some of the basic theory behind the HT and analytic signals. The HT is a linear operator that, for a generic time-varying signal $x(t)$, is defined as [15]:

$$\mathcal{H}[x(t)] = \frac{1}{\pi}\int_{-\infty}^{+\infty}\frac{x(\tau)}{t-\tau}d\tau = \frac{1}{\pi t} * x(t) \tag{1}$$

where $*$ indicates convolution. Combining the HT $\mathcal{H}[x(t)]$ with the original function yields the analytic signal $\hat{x}(t)$ which, due to the symmetry of the spectrum, contains only positive frequency components [15]:

$$\hat{x}(t) = x(t) + \boldsymbol{j}\mathcal{H}(x(t)). \tag{2}$$

Therefore, the HT allows for the construction of the analytic signal and the removal of interference from the negative spectrum, which is prevalent in power system signals since a large portion of the spectral energy is centered around 50 Hz and therefore close to DC. If we apply Euler's formula, the analytic form also allows for the representation of a real time-domain signal as a complex exponential function which has a more mathematically convenient form. Examples of these transformations are shown in the next section.

A. Dictionary Kernels

For power systems, signal dynamics can be generically modeled with the following function and the fundamental frequency f_0, amplitude A_0 and phase φ_0:

$$x(t) = A_0(1 + g_A(t))cos(2\pi f_0 t + g_\varphi(t) + \varphi_0) \tag{3}$$

which has the analytic form:

$$\hat{x}(t) = A_0(1 + g_A(t))e^{\boldsymbol{j}(2\pi f_0 t + g_\varphi(t) + \varphi_0)} \tag{4}$$

where $g_A(t)$ and $g_\varphi(t)$ account for the variation in amplitude and phase, respectively [1]. The FBA algorithm presented in this paper was developed for five common power system dynamics: (i) amplitude modulations, (ii) frequency ramps, (iii) phase modulations, (iv) amplitude steps and (v) phase steps[2]. Each dynamic has a defined parametric model that is transformed into its analytic counterpart using the HT.

Firstly, *amplitude modulations* (AM) typically result from inter-area oscillation events and can be modeled as [16]:

$$x(t,\gamma) = A_0(1 + k_m cos(2\pi f_m t + \varphi_m))cos(2\pi f_0 t + \varphi_0) \tag{5}$$

where f_m is the modulating frequency ($f_m \ll f_0$), φ_m is the phase of modulation and k_m is the depth of modulation. The key parameters can then be represented by $\gamma = [A_0, f_0, f_m, \varphi_0, \varphi_m, k_m]$, while the analytic signal is constructed using (4) and the amplitude and phase variations $g_A(t) = k_m cos(2\pi f_m t + \varphi_m)$ and $g_\varphi(t) = 0$.

The second case concerns *frequency ramps* (FR) which occur in response to faults and large power imbalances and often precede a severe grid collapse. Frequency ramps can be modeled with a ramp rate R in Hz/s, the parameter set $\gamma = [A_0, f_0, \varphi_0, R]$ and the function [16]:

$$x(t,\gamma) = A_0 cos(2\pi f_0 t + R\pi t^2 + \varphi_0). \tag{6}$$

The functions $g_A(t) = 0$ and $g_\varphi(t) = R\pi t^2$ can be used in (4) to create the analytic signal model.

Next we consider *phase modulations* (PM), which also occur during inter-area oscillations and are modeled with a parameter set $\gamma = [A_0, f_0, f_a, \varphi_0, \varphi_a, k_a]$ and the following function:

$$x(t,\gamma) = A_0 cos(2\pi f_0 t + k_a sin(2\pi f_a t + \varphi_a) + \varphi_0). \tag{7}$$

The analytic signal is then defined for $g_A(t) = 0$ and $g_\varphi(t) = k_a sin(2\pi f_a t + \varphi_a)$.

Amplitude steps [AS] frequently occur during faults, load shedding or generator disconnections and can be modeled with a parameter set $\gamma = [A_0, f_0, k_s, t_s, \varphi_0]$ and the function [6]:

$$x(t,\gamma) = A_0(1 + k_s h(t - t_s))cos(2\pi f_0 t + \varphi_0). \tag{8}$$

where k_s is the relative step magnitude, $h(t)$ is the heaviside function and t_s is the location of the step in the window.

[1] Eq. (4) is derived using the property that the HT of the product of two signals with non-overlapping spectra is equal to the product of the low-frequency term and the HT of the high-frequency term. For justification of this assumption see [15].

[2] An extension of the FBA method for extraction of harmonics is also presented in Appendix C.

Consequently, the analytic signal is defined with $g_A(t) = k_s h(t - t_s)$ and $g_\varphi(t) = 0$.

Finally, *phase steps* [PS] are modeled with a parameter set $\gamma = [A_0, f_0, k_p, t_p, \varphi_0]$ and the function [6]:

$$x(t, \gamma) = A_0 cos(2\pi f_0 t + k_p h(t - t_p) + \varphi_0). \tag{9}$$

where k_p and t_p are the step magnitude and location, respectively. Therefore, the analytic signal is defined with $g_A(t) = 0$ and $g_\varphi(t) = k_p h(t - t_p)$.

Using these models, dictionary kernels $\mathbf{d}(t, \gamma)$ for the FBA are computed by finding the Discrete Fourier Transform (DFT) of the analytic signal defined by a given set of parameters γ:

$$\mathbf{d}(t, \gamma) = DFT[\hat{x}(t, \gamma)]. \tag{10}$$

The DFT coefficients for bins $k = 1...L$ are defined as:

$$X(k) = \sum_{l=0}^{L-1} x_l W_L^{kl} \tag{11}$$

where $W_L^k = e^{-j2\pi k/L}$ are the roots of unity. We choose to work in the frequency domain since this allows for the compression of the time-domain signal into a discrete set of Fourier coefficients. The Fourier Transform also acts as a low-pass filter, significantly removing the impact of noise.

B. Dictionary Theory

Choosing a proper dictionary is a critical step in the implementation of the FBA algorithm. Since the objective is to identify the parameters of an unknown signal, an intuitive solution would be to have a uniform grid of the model parameters (e.g., f_0, f_m, φ_m) that spans the allowed space and includes signals for all combinations of values. However, to properly justify this choice, we need to clarify what makes a dictionary effective and how to construct appropriate dictionaries. For this, we look to the fields of sparse modeling and *Compressed Sensing* (CS) [17] which have thoroughly studied the selection, design and optimization of dictionaries.

CS focuses on representing a signal using a linear combination of only a few dictionary atoms (i.e. a sparse representation). More formally, let matrix $\mathbf{D} \in \mathbb{C}^{K \times N}$ be a dictionary of N kernels of length K and $x \in \mathbb{C}^K$ be the given signal. A CS problem then involves solving for a sparse approximation vector α with only a few nonzero elements such that:

$$\hat{\alpha} = \arg\min_{\alpha} ||\alpha||_0 \text{ subject to } ||\mathbf{D}\alpha - x||_2 \leq \varepsilon \tag{12}$$

where ε is a small positive constant. The performance of sparse approximation algorithms is often studied using properties of the dictionary, the most intuitive of which is mutual coherence [17]. *Coherence* of a dictionary indicates the maximum similarity between any two dictionary kernels $(\mathbf{d}_i, \mathbf{d}_j)$ [17]:

$$\mu(\mathbf{D}) = \max_{j \neq i} \frac{|\mathbf{d}_i^H \mathbf{d}_j|}{||\mathbf{d}_i||_2 ||\mathbf{d}_j||_2}, i, j = 1, ...N \tag{13}$$

where H signifies the Hermitian transpose. In designing a dictionary, it is desirable to have kernels with low mutual coherence when solving for a unique sparse representation, as this can reveal underlying structures in the data.

Dictionary selection is commonly performed through either *Dictionary Learning* or *Dictionary Design* [17]. The former adapts an original dictionary to better fit a predefined set of signals. However, this method does not guarantee the kernel structure that we wish to maintain for the FBA algorithm (e.g., AM, FR, PM). The resulting dictionary would contain kernels that have low coherence but are just as unknown as a test signal in terms of parameter and dynamic identification.

Fortunately, methods exist that allow for more precise control and design of the dictionary by incorporating domain knowledge. In particular, the Parametric Dictionary Design (PDD) algorithm allows for the optimization of the dictionary with respect to coherence while maintaining a meaningful parametric model for the kernels [18]. We adapted this method for complex dictionaries and the kernel models discussed in Section II-A in order to better understand and design the structure of optimal dictionaries for the FBA algorithm.

For the sake of nomenclature, a few key terms need to be explained. First, the Gram of dictionary $\mathbf{D}$ is defined as the set of inner products of the columns of $\mathbf{D}$, $\mathbf{G} := \mathbf{D}^H\mathbf{D}$. Therefore, if the kernels of $\mathbf{D}$ are normalized, the magnitude of the diagonal elements of $\mathbf{G}$ is equal to 1 and each off-diagonal element $\mathbf{G}_{i,j}$ is the pairwise coherence of the corresponding kernels $(\mathbf{d}_i, \mathbf{d}_j)$. If the off-diagonal elements of $\mathbf{G}$ are all equal in magnitude, then $\mathbf{D}$ is called an equiangular tight frame (ETF). An ETF is an overcomplete set of N vectors in K dimensional space (where overcompleteness signifies $N > K$) that are maximally separated. The dictionary coherence for an ETF is the minimum for a given set (K, N). For a complex ETF matrix $\mathbf{D} \in \mathbb{C}^{K \times N}$, the off-diagonal elements of the Gram have a fixed magnitude defined as [19]:

$$|\mathbf{G}_{i,j}| = \bar{\mu} = \sqrt{\frac{N - K}{K(N - 1)}}, \forall i \neq j. \tag{14}$$

It is important to note that complex ETFs only exist if $N \leq K^2$ and $N \leq (N - K)^2$ [19]. Furthermore, tight frames are, by definition, overcomplete versions of an orthogonal basis set and therefore have a degree of redundancy since $N > K$ [18]. Consequently, it is desirable to limit the length of the kernels K to a manageable size in order to reduce the number of kernels needed in the dictionary. In the FBA algorithm, each element of kernel $\mathbf{d}_{i,j} \in \mathbb{C}^K$ corresponds to a frequency bin in the spectrum of the analytic signal (10). Since the range of study for power system measurement units in Europe is centered around 50 Hz, much of the spectrum can be trimmed and the kernels can be limited to an appropriate range (e.g., 20 to 80 Hz).

The objective of the PDD algorithm is to find a structured dictionary that is as close as possible to an ETF, and therefore has maximum incoherence. This is achieved by alternatively projecting a parameterized dictionary onto the set Λ^N of Grams for ETFs and then projecting back onto the parameterized dictionary space $\mathcal{D}$. Algorithm 1 provides details on this method. As introduced in Section II-A, the dictionary kernels are parameterized $\mathbf{D}(\Gamma) \in \mathcal{D}$ where $\Gamma \in \mathbb{R}^{p \times N}$ is the parameter matrix with columns γ_i and p parameters (e.g., $\gamma_i = [f_{0,i}, f_{m,i}, \varphi_{m,i}]$ and $p = 3$). The elements of

the kernels are the coefficients of the DFT bins found in (11) and are therefore complex, a feature which changes the implementation of the algorithm described in [18].

To start, the parameter matrix Γ and corresponding dictionary are initialized and the Gram is computed. In step 4, we project the current Gram onto the set of feasible Grams for ETFs Λ^N. For an arbitrary complex matrix Z, the closest Gram in the ETF set is found by setting the diagonal values to 1 and the off-diagonal entries to [19]:

$$g_{i,j} = \begin{cases} z_{i,j}, \text{ if } |z_{i,j}| \leq \bar{\mu} \\ \bar{\mu} e^{\boldsymbol{j}\angle(z_{i,j})}, \text{ otherwise} \end{cases}$$

where $\bar{\mu}$ is the coherence calculated in (14). In step 5, the projection is modified to be partway between the original Gram $\mathbf{G}(\Gamma_m)$ and the projection onto the ETF set $\mathbf{G}_{P_{m+1}}$ with $\alpha = 0.5$. The resulting Gram $\mathbf{G}_{R_{m+1}}$ is therefore more similar in structure to the dictionary set $\mathcal{D}$, making the projection onto this set in step 6 easier [18]. The projection onto the dictionary set $\mathcal{D}$ is found by applying *Gradient Descent* (GD) to the following optimization problem [18]:

$$\min_{\Gamma} \Phi(\Gamma), \Phi(\Gamma) := ||\mathbf{D}(\Gamma)^H \mathbf{D}(\Gamma) - \mathbf{G}_{R_{m+1}}||_F^2. \tag{15}$$

The objective function $\Phi(\Gamma)$ is, in general, non-convex, and is minimized here by implementing the following GD updates to Γ for iterations $h = 1...H$ and step size ϵ:

$$\Gamma_{m+1}^{[h+1]} = \Gamma_m^{[h]} - \epsilon \nabla_\Gamma \Phi \Big|_{\Gamma_m^{[h]}}. \tag{16}$$

When deriving the gradient of the objective function, it is convenient to separate the real and imaginary components such that the complex dictionary and Gram are defined as $\mathbf{D} = \mathbf{D}_{Re} + \boldsymbol{j}\mathbf{D}_{Im}$ and $\mathbf{G} = \mathbf{G}_{Re} + \boldsymbol{j}\mathbf{G}_{Im}$, respectively, where the complex Gram $\mathbf{G}$ is Hermitian ($\mathbf{G}^H = \mathbf{G}$). The objective function can then be rewritten as:

$$\begin{aligned} \Phi(\Gamma) :=& ||(\mathbf{D}_{Re}^T - \boldsymbol{j}\mathbf{D}_{Im}^T)(\mathbf{D}_{Re} + \boldsymbol{j}\mathbf{D}_{Im}) - (\mathbf{G}_{Re} + \boldsymbol{j}\mathbf{G}_{Im})||_F^2 \\ =& ||\mathbf{D}_{Re}^T\mathbf{D}_{Re} + \mathbf{D}_{Im}^T\mathbf{D}_{Im} - \mathbf{G}_{Re}||_F^2 + \\ & ||\mathbf{D}_{Re}^T\mathbf{D}_{Im} + \mathbf{D}_{Re}^T\mathbf{D}_{Im} - \mathbf{G}_{Im}||_F^2. \end{aligned} \tag{17}$$

The gradient of the objective is found using the Jacobian chain rule:

$$\nabla_\Gamma \Phi = \frac{\partial \mathbf{D}_{Re}}{\partial \Gamma} \frac{\partial \Phi}{\partial \mathbf{D}_{Re}} + \frac{\partial \mathbf{D}_{Im}}{\partial \Gamma} \frac{\partial \Phi}{\partial \mathbf{D}_{Im}}. \tag{18}$$

Algorithm 1 Parametric Dictionary Design [18]

1: **Initialization:** m=1, $\mathbf{D}(\Gamma_1) \in \mathcal{D}$
2: **while** $m \leq M$ **do**
3: $\quad \mathbf{G}(\Gamma_m) = \mathbf{D}(\Gamma_m)^H \mathbf{D}(\Gamma_m)$
4: $\quad \mathbf{G}_{P_{m+1}} = min_{\mathbf{G} \in \Lambda^N} ||\mathbf{G}(\Gamma_m) - \mathbf{G}||_F$
5: $\quad \mathbf{G}_{R_{m+1}} = \alpha \mathbf{G}_{P_{m+1}} + (1-\alpha)\mathbf{G}(\Gamma_m)$
6: $\quad \mathbf{D}(\Gamma_{m+1}) \in \mathbf{D}(\Gamma_m) \cup \{\forall \mathbf{D} \in \mathcal{D} : ||\mathbf{D}^H\mathbf{D} - \mathbf{G}_{R_{m+1}}||_F < ||\mathbf{G}(\Gamma_m) - \mathbf{G}_{R_{m+1}}||_F\}$
7: $\quad m = m + 1$
8: **end while**

For derivations of $(\nabla_{\mathbf{D}_{Re}}\Phi, \nabla_{\mathbf{D}_{Im}}\Phi)$ and $(\nabla_\Gamma \mathbf{D}_{Re}, \nabla_\Gamma \mathbf{D}_{Im})$, see Appendix A. In practice, the GD algorithm and outer loop (Algorithm 1) are implemented for H and M iterations, respectively, or until the dictionary parameters exceed the boundary conditions.

Implementing PDD for each of the signal models discussed in Section II-A, we can observe how the parameters evolve during the iterations. For instance, when optimizing a dictionary of frequency ramps, we observe that the parameters spread uniformly within the allowed parameter space. However, for signal dynamics where the fundamental frequency is dominant (e.g., amplitude modulations), it is useful to fix all parameters except for one and optimize over the free parameter. When this is done, it is observed that the free variable will spread uniformly across the parameter range. These results verify that a low coherence dictionary of AM, FR, AS, PS or PM spectra is one that contains almost uniformly distributed parameters and can therefore be defined with a parameter grid for fixed parameter resolutions and ranges.

C. Dictionary Design

Based on the results of the last section, the dictionaries used for the remainder of this paper are defined by the resolution (or cardinality) and the range of each parameter set. As a useful visual, the dictionary is organized into tensors of rank $(p+1)$ for p parameters, an alternative form to the one in Sec. II-B. Dimensions 1 through p correspond to the parameter sets while the $(p+1)$ dimension contains the kernels. For example, a FR dictionary can be defined as a rank 3 tensor $\mathbf{D} \in \mathbb{C}^{n_{f_0} \times n_R \times K}$, where n_{f_0} and n_R are the number of different fundamental frequencies and ramp rates, respectively. A specific dictionary kernel $\mathbf{d}_{i,j} \in \mathbb{C}^K$, containing K frequency bins, is identified in Fig. 1 for a given f_0^i and R^j.

III. Functional Basis Analysis

In this section, we provide details on the proposed algorithm. For each signal dynamic, a dictionary is built offline and composed of kernels for a given parameter set γ, as discussed in Section II. The steps for estimating the signal parameters are described in Algorithm 2, specifically for a dictionary with $p = 2$ parameters where n_1 and n_2 are the cardinality of the respective parameter sets.

We are given a sampled signal $x(t_l)$ for $l = 1...L$. Since the mathematical model of the signal is unknown, the analytic form $\hat{x}(t_l)$ first needs to be approximated in step 2 by means

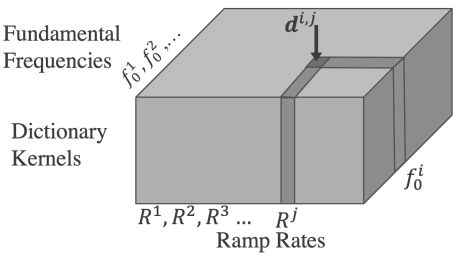

Fig. 1. Visual of a FR dictionary $\mathbf{D}$ characterized by parameters f_0 and R.

of a filter with a magnitude response of nearly 0 for positive frequencies and large attenuation (e.g., -120 dB) for the negative frequency domain.

In steps 3-4, the frequency spectrum $\hat{X}_{full}$ of the analytic signal is computed and curtailed such that only bins in the desired frequency range remain (e.g., 20 to 80 Hz)[3]. This range is selected to analyze the transients detailed in Section II-A but could be modified to extract higher frequency components (see Appendix C for an example of harmonic detection).

In step 5, we project the resulting trimmed frequency spectrum $\hat{X}$ onto each atom $\mathbf{d}_{i,j}$ in the dictionary which yields a complex coefficient of the projection $c_{i,j}$. The coefficient is used to scale and rotate the kernel for evaluation of the residual $e_{i,j}$ in step 6 with $\mathbf{E} \in \mathbb{R}^{n_1 \times n_2}$ representing the matrix of residuals $e_{i,j}$ for all kernels. In steps 7-8, the kernel with the smallest residual in $\mathbf{E}$ is identified and the corresponding parameters γ_1 are used as the initial guess for a GD algorithm.

For steps 9-14, GD is used to optimize the model parameters such that the objective function, defined in step 10 (i.e., the difference between the true spectrum $\hat{X}$ and the kernel spectrum $\mathbf{d}(\gamma)$), is minimized in each update (step 12). For clarity, let $C(\gamma) = \mathbf{d}(\gamma)^H \hat{X} \mathbf{d}(\gamma) - \hat{X}$ and $\Psi(\gamma) = C(\gamma)^H C(\gamma)$. The objective can then be framed as:

$$\Phi(\gamma) = \|\mathbf{d}(\gamma)^H \hat{X} \mathbf{d}(\gamma) - \hat{X}\|_2 = \|C(\gamma)\|_2 \tag{19}$$

$$= \sqrt{C(\gamma)^H C(\gamma))} = \sqrt{\Psi(\gamma)}. \tag{20}$$

Algorithm 2 Functional Basis Analysis

1: **Input:** signal $x(t_l)$, dictionary $\mathbf{D}$
Projection:
2: $\hat{x}(t_l) = x(t_l) + jH(x(t_l))$ =filter$[x(t_l)]$
3: $\hat{X}_{full} = DFT[\hat{x}(t_l)]$
4: $\hat{X} = \text{trim}[\hat{X}_{full}]$
5: $c_{i,j} = \mathbf{d}_{i,j}^H \hat{X}$, $i = 1, ..., n_1$ and $j = 1, ..., n_2$
6: $e_{i,j} = ||c_{i,j}\mathbf{d}_{i,j} - \hat{X}||_2$
7: $[i^*, j^*] = \arg\min[E]$
8: $\gamma_1 = \Gamma(i^*, j^*)$
GD loop:
9: Initialization: $m = 1$, $1 \leq M$, $\epsilon \in \mathbb{R}^+$,
10: $\Phi(\gamma_m) = \|\mathbf{d}(\gamma_m)^H \hat{X} \mathbf{d}(\gamma_m) - \hat{X}||_2$
11: **while** $m \leq M$ **or** $|\Phi_{m+1} - \Phi_m| > \varepsilon$ **do**
12: $\quad \gamma_{m+1} = \gamma_m + \epsilon_m \nabla_\gamma \Phi\big|_{\gamma_m}$
13: $\quad m = m + 1$
14: **end while**
15: $\gamma^* = \gamma_m$
16: Reconstruct signal: $\tilde{x}(t_l) =$ dynamic model (γ^*)
17: Compute Time-Domain Error

The derivation of the gradient of the objective with respect to the parameters is presented in Appendix B. It is also important to note that the selection of the step size ϵ_m is not trivial. This is formulated as an internal optimization loop where the step size is adaptively chosen for each iteration m to minimize the objective function. For Algorithm 2, a backtracking line-search is implemented such that the step size is iteratively decreased by $\epsilon = \beta\epsilon$ where $\beta \in (0, 1)$. The step size is shrunk until it adequately reduces the objective function, satisfying the exit inequality [20]:

$$\Phi(\gamma + \epsilon\Delta\gamma_m) \leq \Phi(\gamma_m) + \alpha\epsilon\nabla_{\gamma_m}\Phi^T\Delta\gamma_m \tag{21}$$

with control parameters β and $\alpha \in (0, 0.5)$, and descent direction $\Delta\gamma_m = -\nabla_{\gamma_m}\Phi$. As this is a non-convex problem, the solution found may be a local minimum[4].

GD is terminated after a fixed number of iterations or after the change in the objective function is below a predetermined limit ε. Once completed, the final set of parameters γ^* is used to reconstruct the original signal (step 16). The dynamic model from the dictionary, as discussed in Section II-A, is computed for γ^* and the time period defined by the window. The estimated fundamental amplitude and phase are not included in the parameter set γ but instead are determined from the coefficient of the projected true signal spectrum onto the predicted signal spectrum[5]:

$$c^* = \mathbf{d}(\gamma^*)^H \hat{X} \rightarrow A_0^* = |c^*|, \varphi_0^* = \angle c^*. \tag{22}$$

The Time-Domain Error (TDE), defined as:

$$TDE = \frac{||\tilde{x}(t_l) - x(t_l)||_2}{\sum_{l=1}^{L} x(t_l)^2}, \tag{23}$$

is then computed in step 17 to evaluate the accuracy of the reconstruction[6]. It should be noted that, in a real-world scenario where the true parameters of the signal are unknown, the TDE is the only available metric for performance evaluation.

A. Identification of Multi-Dynamic Signals

Some care must be taken when identifying which dynamics are present in the signal. As discussed in Section II-B, the dictionaries are designed such that the coherence of kernels in a given dictionary (e.g., AM, PM, FR, AS, PS) is reduced. However, the coherence of the dictionaries is larger than zero (i.e., not an orthogonal basis) and therefore it is possible for the projection of a signal onto this functional set to yield multiple solutions with similar residuals, TDEs and spectra.

To complicate matters, some dynamics are similar and easily misidentified and, in the case of multi-dynamics, the detection of the proper combination can be challenging. Ideally, we would like to perform, in parallel, the dictionary projection and optimization of the signal for each dynamic model, and compare the resulting TDE to determine which dynamic is present. However, this strategy fails when multiple dynamics are involved. For instance, feeding an AM/FR signal into a FR dictionary will yield inaccurate estimations of the FR due to the AM distortions of the spectrum.

[3]Note that the curtailed spectrum $\hat{X}$ is made to have a unit norm. This is because the GD steps and the original dictionary are designed for normalized kernels with magnitudes of 1.

[4]The assessment of the global minimum of the objective is beyond the scope of this paper.

[5]For this projection to yield the appropriate amplitude, the original and predicted signal spectra, calculated by (11), should be normalized by the signal length, L.

[6]This metric is normalized by the energy present in the signal window so that consecutive estimations can be compared.

Instead, we propose the heuristic Algorithm 3 that leverages some observed properties of the dictionaries and the signal dynamics. Specifically, the AM, AS and PS dictionaries can reliably extract an estimate of the parameters characterizing discontinuities or modulations, even in the presence of other dynamics. Furthermore, when the FR or PM dictionary kernels include the appropriate fixed AM or AS component, accurate estimations of the other dynamic parameters can be found.

Algorithm 3 Signal Characterization via FBA

1: **Input:** Signal $\hat{x}(t_l)$,
Dictionaries $\mathbf{D}_{AM}$, $\mathbf{D}_{PM}$, $\mathbf{D}_{FR}$, $\mathbf{D}_{AS}$, $\mathbf{D}_{PS}$, $\mathbf{D}_{SS}$
2: $\hat{X}_{full} = DFT[\hat{x}(t_l)]$
3: $\hat{X} = \text{trim}[\hat{X}_{full}]$
AM, PM, FR, AS, PS, and SS detection:
4: Algorithm 2 (AM):
$\rightarrow \gamma^*_{AM} = [f^*_{0,AM}, f^*_{m,AM}, \varphi^*_{m,AM}]$, TDE_{AM}
5: Algorithm 2 (PM):
$\rightarrow \gamma^*_{PM} = [f^*_{0,PM}, f^*_{a,PM}, \varphi^*_{a,PM}]$, TDE_{PM}
6: Algorithm 2 (FR):
$\rightarrow \gamma^*_{FR} = [f^*_{0,FR}, R^*_{FR}]$, TDE_{FR}
7: Algorithm 2 (AS):
$\rightarrow \gamma^*_{AS} = [f^*_{0,AS}, k^*_{s,AS}, t^*_{s,AS}]$, TDE_{AS}
8: Algorithm 2 (PS):
$\rightarrow \gamma^*_{PS} = [f^*_{0,PS}, k^*_{p,PS}, t^*_{p,PS}]$, TDE_{PS}
9: Algorithm 2 (SS):
$\rightarrow \gamma^*_{SS} = [f^*_{0,SS}]$, TDE_{SS}
AS/PM, AS/FR and AS/PS detection:
10: **if** $k_{s,AS} \neq 0$ **then**
11: $\mathbf{D}_{AS/PM} = \mathbf{D}_{PM}(k^*_{s,AS}, t^*_{s,AS})$
12: $\mathbf{D}_{AS/FR} = \mathbf{D}_{FR}(k^*_{s,AS}, t^*_{s,AS})$
13: Algorithm 2 (AS/PM):
$\rightarrow \gamma^*_{AS/PM} = [f^*_0, k^*_s, t^*_s, f^*_a, \varphi^*_a]$, $TDE_{AS/PM}$
14: Algorithm 2 (AS/FR):
$\rightarrow \gamma^*_{AS/FR} = [f^*_0, k^*_s, t^*_s, R^*]$, $TDE_{AS/FR}$
15: AS/PS:
$\rightarrow \gamma^*_{AS/PS} = [f^*_{0,PS}, k^*_{s,AS}, t^*_{s,AS}, k^*_{p,PS}, t^*_{p,PS}]$
$TDE_{AS/PS}$
16: **end if**
AM/PM, AM/FR and AM/PS detection:
17: **if** $f^*_{m,AM} \neq 0$ **then**
18: $\mathbf{D}_{AM/PM} = \mathbf{D}_{PM}(f^*_{m,AM}, \varphi^*_{m,AM})$
19: $\mathbf{D}_{AM/FR} = \mathbf{D}_{FR}(f^*_{m,AM}, \varphi^*_{m,AM})$
20: Algorithm 2 (AM/PM):
$\rightarrow \gamma^*_{AM/PM} = [f^*_0, f^*_m, \varphi^*_m, f^*_a, \varphi^*_a]$, $TDE_{AM/PM}$
21: Algorithm 2 (AM/FR):
$\rightarrow \gamma^*_{AM/FR} = [f^*_0, f^*_m, \varphi^*_m, R^*]$, $TDE_{AM/FR}$
22: AM/PS:
$\rightarrow \gamma^*_{AM/PS} = [f^*_{0,PS}, f^*_{m,AM}, \varphi^*_{m,AM}, k^*_{p,PS}, t^*_{p,PS}]$
$TDE_{AM/PS}$
23: **end if**
24: $dynamic = \arg\min(TDE_{dynamics})$
25: $\gamma^* = \gamma_{dynamic}$

To reduce computation time, dictionaries for AM, PM, FR, AS, PS and Steady State (SS) conditions are pre-computed and stored. Once the input analytic signal $\hat{x}(t_l)$ is properly transferred into the frequency domain (steps 2 and 3), steps 4-9 are performed to identify AM, PM, FR, AS, PS and SS signals. Algorithm 2 is executed in parallel for each of these dynamics and the resulting estimated parameters and TDE are recorded. If a sufficiently large AS is detected, steps 10-15 are completed to identify combinations of amplitude steps and PM, FR and PS dynamics. The FR and PM dictionaries are adapted in steps 11 and 12 to incorporate the amplitude step term: $(1 + k_s h(t - t_s))$. Two versions of Algorithm 2 are then performed in parallel using the modified dictionaries $\mathbf{D}_{AS/FR}$ and $\mathbf{D}_{AS/PM}$. In steps 13 and 14, the full set of parameters are optimized for both AS/PM and AS/FR dynamics and the resulting TDE are computed. Note that, in step 15, the AS/PS waveform is reconstructed using the parameters identified by analysis of the separate dynamics (steps 7 and 8) rather than a combined dynamic dictionary. As discussed previously, AS, PS and AM dictionaries are capable of accurately extracting parameters even in the presence of other dynamics.

Similarly, if AM is detected, steps 17-22 are performed to identify the multi-dynamic signals AM/PM, AM/FR and AM/PS. The amplitude modulation term $(1 + k_m cos(2\pi f^*_{m,AM} t + \varphi^*_{m,AM}))$ is embedded into the FR and PM dictionaries and the parameters are optimized in steps 20-21. As discussed above, the AM/PS waveform is estimated in step 22 using parameters from analysis of the AM and PS dynamics (steps 4 and 8). Finally, the signal dynamic corresponding to the smallest TDE is identified and its parameters are reported as the final solution (steps 24 and 25).

It is important to note that the simultaneous presence of significant FR and PM dynamics, though rare, is exceptionally difficult to identify, particularly for short window lengths. Indeed, for short observation periods, the time- and frequency-domain of PMs and FRs can be almost indistinct, particularly for slow modulations. Therefore, discriminating between PMs and FRs in a 60 ms window is challenging and the identification of PM/FR is significantly more so. However, it should be noted that, although PM, FR or PM/FR may be misidentified, the FBA algorithm will anyhow reconstruct a signal with low TDE, as demonstrated in Section IV. With a longer window, it may be possible to differentiate between these dynamics. However, the trade-off between longer windows and latency is a compromise that must be made by the designer.

B. Computational Complexity

The proposed algorithm has been developed for eventual implementation in typical microcontroller architectures used in PMUs, like FPGA-based (Field Programmable Gate Array) devices. For this reason, the algorithm should be programmed optimally. The computational complexity of the overall algorithm is dependent on the number of dictionary kernels N, frequency bins K, samples in the input signal L, and parameters in the model p. The gradient descent iterations M and steps for the backtracking line-search Q also impact the complexity. We will represent the computational complexity of the DFT calculation as $\xi(K, L)$ for simplicity.

While each dictionary projection in Algorithm 3 is an $\mathcal{O}(KN)$ procedure, the projection onto the single dynamic

dictionaries (e.g., AM, SS, FR) can be done in parallel. Similarly, the optimization of the parameters for each dynamic can be parallelized and costs $\mathcal{O}(M((Q+p)\xi+QL))$. If necessary, the creation of combined dynamic dictionaries could also be done in parallel, requiring $\mathcal{O}(N(\xi+L))$ operations. Projection onto the dictionaries and optimization of the parameters for the combined signal dynamic models (e.g., AM/PM, AS/FR) would take a total of $\mathcal{O}(KN)$ and $\mathcal{O}(M((Q+p)\xi+QL))$ operations, respectively, when performed in parallel. Regarding the computation of the DFT coefficients, the Fast Fourier Transform function is characterized by a complexity of $\xi = \mathcal{O}(Llog_2(L))$. However, since only K of the frequency bins are required a direct calculation of the coefficients for the specific bins would be less expensive, costing only $\xi = \mathcal{O}(KL)$. This could be made even more efficient using methods like MSDFT where the Fourier coefficients of desired frequency bins are calculated using previous calculations and therefore needing only $\xi = \mathcal{O}(17K)$ operations [21].

IV. Performance Assessment

In this section, the proposed FBA method's capacity to identify dynamic signals typical in power systems is evaluated. In IV-A, we explore the benefits and limitations of the algorithm for different window lengths. In IV-B, we compare the performance of the algorithm to both standard and dynamic phasor-based methods as a function of the modulating frequency, step size or ramp rate of the dynamic. Finally, in IV-C, the FBA algorithm is applied to waveforms adapted from real-world grid events.

For all tests, the FBA dictionaries are defined by the resolutions and ranges in Table I and the following parameter sets: $\gamma_{AM} = [f_0, f_m, \varphi_m]$, $\gamma_{PM} = [f_0, f_a, \varphi_a]$, $\gamma_{FR} = [f_0, R]$, $\gamma_{AS} = [f_0, k_s, t_s]$, and $\gamma_{PS} = [f_0, k_p, t_p]$ with k_m and k_a fixed at 0.1. The ranges in Table I were selected to capture common transients observed in the real-world, based on the dynamic tests described in the IEEE Standard C37.118 [22]. As discussed in Sections II-B and II-C, the coherence of the dictionary kernels is reduced by uniformly spacing the model parameters within the parameter ranges. Therefore, the resolutions were chosen based on the algorithm's performance and the computational cost. A higher resolution parameter set reduces the likelihood of identifying a local rather than global minimum in Algorithm 2, but increases the computational burden of projecting the input signal onto the dictionary.

For the tests in Sections IV-A and IV-B, and in order to have better control and knowledge of the true dynamic, synthetic signals are created using models of the dynamics of interest discussed in Section II-A. Because the model of these signals is known, the filter in step 2 of Algorithm 2 is unnecessary and we can compute the analytic signal directly using the equations presented in Section II-A. The signals are generated with a sampling frequency of 5 kHz for a parameter set and duration defined by each test and described in the following sections.

TABLE I
Parameter sets for FBA dictionaries

Parameter	Resolution	Range
f_0	0.02 Hz	[49,51] Hz
f_m, f_a	0.1 Hz	[0,5] Hz
φ_m, φ_a	0.13 rad	[0, 2π] rad
R	0.1 Hz/s	$\pm$[0.2, 5] Hz/s
k_s, k_p	0.01	$\pm$[0.1,0.8],[$\pi/18, 5\pi/18$]
t_s, t_p	0.4 ms	$[10, T_w - 10]$ ms

TABLE II
60 ms window: Mean TDE and Maximum FE and RFE for signal dynamic tests using the FBA algorithm.

Signal Dynamic	Max FE (mHz)	FE Limit (mHz)	Max RFE (mHz/s)	RFE Limit (mHz/s)	Mean TDE
SS	0.1	5	2	10	8.20E-06
AM	0.9	60	32	2300	9.90E-06
FR	5	10	147	200	1.00E-05
PM	8	60	112	2300	1.30E-05
AS	4	-	0	-	1.16E-03
PS	31	-	0	-	1.00E-03
AM/FR	2	-	223	-	1.40E-05
AM/PM	8	60	276	3000	1.90E-05
AM/PS	57	-	0	-	1.32E-03
AS/FR	24	-	280	-	1.10E-03
AS/PM	17	-	330	-	1.20E-03
AS/PS	100	-	0	-	3.80E-03

Several metrics are used to evaluate the algorithm's performance, including the TDE in (23) and the parameter error defined for each parameter as: $\gamma_{error} = |\gamma_{true} - \gamma_{est}|$. Additionally, in order to compare the FBA method to state-of-the-art measurement techniques in power systems, we make reference to the current standard for synchrophasor estimation, IEEE Std C37.118 [22]. In particular, we consider frequency error (FE) and the rate of change of frequency error (RFE). Traditionally, these metrics represent the deviation of the phasor estimated frequency and ROCOF from the true instantaneous frequency and ROCOF at the reporting time, conventionally located at the center of the window.

A. Window Sensitivity and Parameter Estimation Accuracy

For a comprehensive evaluation of the FBA algorithm's performance, tests are conducted on a variety of signal dynamics. For each dynamic type, 500 signals are generated with 80 dB of white Gaussian noise for $T_w = 60$ ms and 200 ms periods, with parameters randomly selected from within specified ranges.

- Dynamics: SS, AM, PM, FR, AS, PS, AS/FR, AS/PM, AS/PS, AM/PS, AM/PM and AM/FR.
- Parameter ranges: $f_0 \in [49, 51]$ Hz, $(f_m, f_a) \in [0, 5]$ Hz, $R \in [-5, 5]$ Hz/s, $(\phi_m, \phi_a) \in [0, 2\pi]$ rad, $k_s \in \pm[0.1, 0.8]$, $k_p \in \pm[\pi/18, 5\pi/18]$ and $(t_s, t_p) \in [0.01, T_w - 0.01]$ s.

The mean parameter errors and TDE and maximum FE and RFE are reported for the different window sizes in Tables II and III. The limits for the PMU tests detailed in IEEE Std C37.118 are provided for reference in Table II.

As previously discussed, a 60 ms window is frequently too short to distinguish between FRs and PMs as the time-domain evolution of the frequency dynamic is nearly identical within such an observation interval. Although misidentified signals yield invalid parameter estimations, the time and frequency

TABLE III
200 MS WINDOW: MEAN PARAMETER ERROR AND TDE AND MAXIMUM FE AND RFE FOR SIGNAL DYNAMIC TESTS USING THE FBA ALGORITHM.

Signal Dynamic	Mean Parameter Error											Max FE	Max RFE
	f_0 (mHz)	f_m (mHz)	ϕ_m (rad)	f_a (mHz)	ϕ_a (rad)	R (mHz/s)	t_s (ms)	k_s (%)	t_p (ms)	k_p (%)	TDE		
SS	0.2	-	-	-	-	-	-	-	-	-	4.50E-06	0.016	1.2
AM	0.2	3.5	0.02	-	-	-	-	-	-	-	5.70E-06	0.1	6
PM	5	-	-	58	0.16	-	-	-	-	-	1.80E-05	4.7	222
FR	14	-	-	-	-	48	-	-	-	-	2.40E-04	13	420
AS	1	-	-	-	-	-	1.5	2.6	-	-	5.20E-04	1.3	0
PS	3.5	-	-	-	-	-	-	-	0.511	0.45	8.80E-04	11	0
AM/PM	4	45	0.08	76	0.14	30	-	-	-	-	3.70E-05	3	196
AM/FR	13	39	0.04	-	-	-	-	-	-	-	3.70E-05	18	498
AM/PS	4	62	0.12	-	-	-	-	-	0.57	0.93	9.30E-04	13	0
AS/PM	11	-	-	72	0.135	-	0.535	1.1	-	-	1.00E-03	33	560
AS/FR	3.3	-	-	-	-	34	0.59	1.23	-	-	1.20E-03	18	146
AS/PS	6.4	-	-	-	-	-	1.29	2.86	0.77	1.28	2.00E-03	109	0

domain reconstructions are extremely accurate for a 60 ms window. For this reason, only the FE, RFE and TDE are presented for this window size in Table II.

Indeed, with a 60 ms window, the maximum FE and RFE found for the generated cases are well within the limits specified by the standard. Furthermore, the mean TDE is consistent across all dynamics, with AS and PS being the exception due to the presence of an abrupt discontinuity. Observe that the RFE for these step discontinuities is 0 Hz/s since the model correctly assumes that there is no frequency variation present in the window. With a 200 ms window, as shown in Table III, the FBA method accurately extracts the parameters of the signal and distinguishes between most dynamics, although slow FRs are occasionally mistaken for PMs. Note that even in cases where a step in the amplitude and phase occurs in the same window (AS/PS) at different locations and magnitudes, the FBA method can accurately identify the dynamic and estimate the step parameters and the underlying frequency.

B. Comparison with Phasor-based Algorithms

In this section, the performance of the proposed algorithm is compared with both standard and dynamic phasor estimation methods. For the former, we selected a 2-point iterative Interpolated DFT (i-IpDFT) algorithm with a Hann window and negative spectrum compensation which is compliant with P and M class requirements [23]. For the dynamic phasor method, we employed the Compressed Sensing Taylor-Fourier multifrequency (CSTFM) method [12] which captures the 1^{st} and 2^{nd} order derivatives of the phasor.

The following dynamic cases are analyzed:

- Amplitude modulations: characterized by $f_0 = 50$ Hz and modulating frequencies spanning $f_m \in [0.1, 5]$ Hz.
- Phase modulations: characterized by $f_0 = 50$ Hz and modulating frequencies spanning $f_a \in [0.1, 5]$ Hz.
- Frequency ramps: characterized by $f_0 = 49$ Hz with ramp rates $R \in [0.1, 5]$ Hz/s or $f_0 = 51$ Hz with ramp rates $R \in [-5, -0.1]$ Hz/s.
- Amplitude steps: characterized by $f_0 = 50$ Hz and $k_s \in \pm[0.1, 0.8]$.
- Phase steps: characterized by $f_0 = 50$ Hz and $k_p \in \pm[\pi/18, 5\pi/18]$.

Each signal is generated for the given dynamic and parameter set for a duration of 5 s. 80 dB of white noise is added and a 60 ms sliding window with a reporting rate of 50 fps is applied. Note that the FR tests are halted when the frequency exceeds the boundaries of the dictionary (i.e.,$[49, 51]$ Hz) and the step tests are stopped when the transient is cleared. For each signal, the worst case FE and TDE are recorded and the results are presented in Fig. 2, 3, 4, 5 and 6.

It is worth noting that FE is a metric designed for phasor estimates. Since a computed phasor is essentially an average of the signal dynamic present in the window and the FE compares the frequency estimated for the center of the window, this error is generally low for dynamics with linear changes in frequency. However, while the frequency at the reporting time (i.e., the center of the window) may be well aligned with the phasor frequency, the steady-state assumption is invalid for the rest of the window. This limitation is reflected in the TDE metric which indicates the suitability of the reconstructed signal across the full window, without relying on static assumptions as is the case with FE and total vector error (TVE) [22].

In Fig. 2, we see how modulations in the amplitude can significantly distort the phasor estimates found by the i-IpDFT algorithm. Indeed, the worst case FE and TDE for i-IpDFT increase with the magnitude of the modulation, eventually exceeding the IEEE standard limit of 60 mHz. CSTFM can cope with amplitude modulations better and therefore displays improved FE (though it is sometimes unreliable and can result in large errors as observed at $f_m = 1.5$ Hz). For faster amplitude modulations, however, the dynamic phasor is unable to capture the signal dynamic properly, which is reflected by the increase in both the FE and TDE. The performance of the FBA algorithm, in contrast, is not affected by the modulation. In fact, the time and frequency error metrics stay relatively steady for all values of f_m and show that the FBA algorithm consistently outperforms both the i-IpDFT and dynamic phasor methods for faster AM dynamics.

The results of the FR tests for ramp rates between -5 and 5 Hz/s are shown in Fig. 3. All methods perform well within the P class limit of 10 mHz for FR tests [22]. While the i-IpDFT and CSTFM methods have comparable performance to the FBA algorithm in terms of FE, we again need to remember the limitations of the FE metric in describing dynamics. As

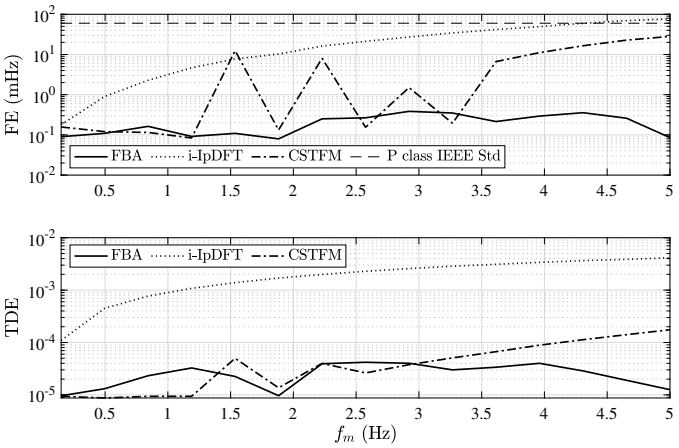

Fig. 2. Amplitude Modulation test: Worst-Case FE and TDE for i-IpDFT, CSTFM and FBA methods as a function of the modulating frequency. The dashed line represents the IEEE Standard limit of 60 mHz for AM tests.

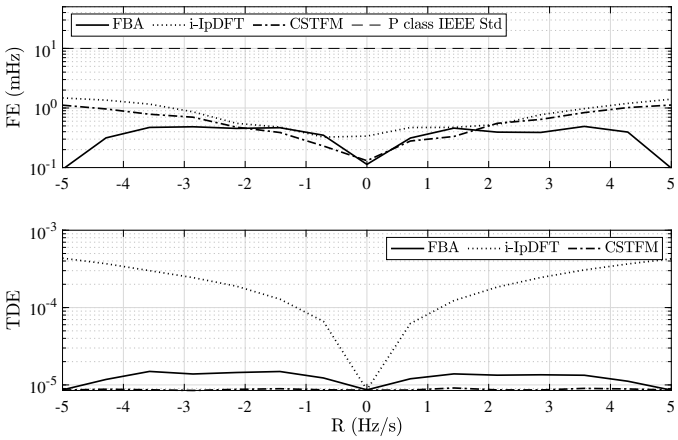

Fig. 3. Frequency Ramp test: Worst-Case FE and TDE for i-IpDFT, CSTFM and FBA methods as a function of the ramp rate. The dashed line represents the IEEE Standard limit of 10 mHz for FR tests.

demonstrated by the TDE curves in Fig. 3, the reconstructed frequency and signal are better matched by the FBA method, which tracks the full frequency dynamic rather than just the average. The TDE for the FBA method is low for all ramp rates while the i-IpDFT error increase with the ramp rate R. Since the frequency change is linear, the CSTFM algorithm can sufficiently capture the waveforms and, for all ramp rates, has similar performance to the FBA method.

The results for the PM tests, shown in Fig. 4, demonstrate a similar trend. The FE for all methods is comparable, with values ranging from less than 1 mHz up to 10 mHz, well below the IEEE limit of 60 mHz. Since most PMs viewed by a 60 ms window resemble frequency ramps, the averaged frequency found with a phasor estimation algorithm closely matches the true frequency at the center of the window, as was the case with the FR tests. However, the FBA method shows a clear improvement over the i-IpDFT algorithm in terms of TDE since the overall frequency trend present in the window is better matched. As was the case with AM, the TDE for the CSTFM method begins to diverge for faster modulations.

Amplitude and phase steps are particularly challenging dynamics for phasor extraction algorithms. Indeed, Fig. 5 and 6 demonstrate how poorly the i-IpDFT and CSTFM algorithms perform in the presence of amplitude or phase steps with increasing relative magnitudes. The FE estimated by these methods can be in the order of several *Hz* when the step change occurs in the center of the observation window. In contrast, the FBA method is capable of capturing and characterizing these signal dynamics and yields relatively small frequency and time-domain errors. Indeed, the algorithm can accurately track the movement of steps through the observation window while maintaining an excellent estimate of the signal's frequency.

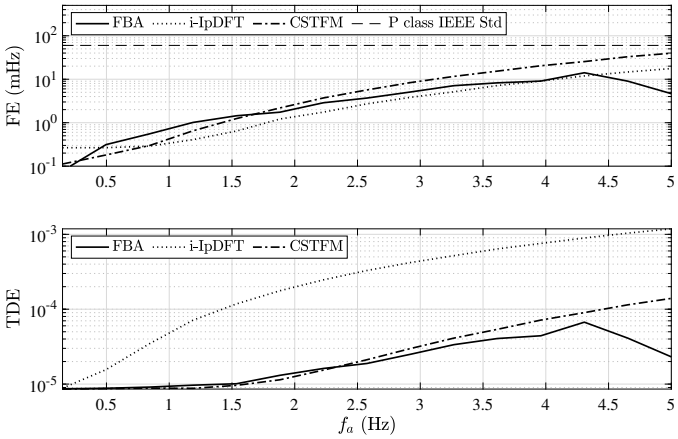

Fig. 4. Phase Modulation test: Worst-Case FE and TDE for i-IpDFT, CSTFM and FBA methods as a function of the modulating frequency. The dashed line represents the IEEE Standard limit of 60 mHz for PM tests.

C. Real-World Signals

In this section, two waveforms from real grid events are analyzed with the FBA, i-IpDFT and CSTFM dynamic phasor methods. Since the ground truth values of the underlying signal dynamic are unknown, the TDE for the overlapping observation windows is the only indicator of how well the

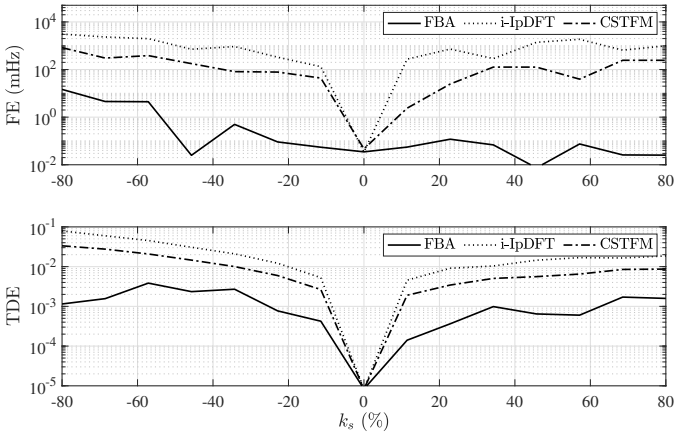

Fig. 5. Amplitude Step test: Worst-Case FE and TDE for i-IpDFT, CSTFM and FBA methods as a function of the step magnitude.

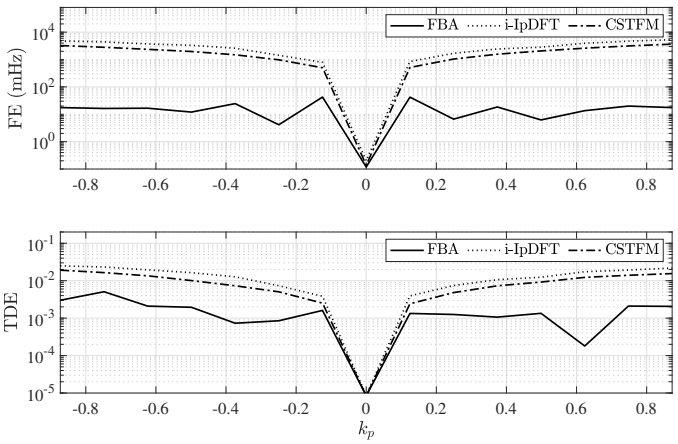

Fig. 6. Phase Step test: Worst-Case FE and TDE for i-IpDFT, CSTFM and FBA methods as a function of the step magnitude.

reconstructed waveform matches the input signal. For this analysis, a 60 ms window is used with a 50 fps reporting rate and the FBA dictionaries defined by Table I. The analytic signal of the waveform is computed using a filter of order 31 and a transition width set to 50π radians per sample in order to comply with PMU-based applications [6].

The first case involves a voltage sag that occurred at the input power of the MWPI paper manufacturing plant as the result of a short circuit in the one of the plant's transformers [24]. A current waveform from the event is analyzed and the resuling TDE for each method is displayed in Fig. 7. Note that the bottom two graphs show the TDE and signal dynamic parameters at the reporting times which are aligned with the start of the observation window (e.g., the TDE at 0.2 s corresponds to the window from 0.2 s to 0.8 s). From 0 s to 0.13 s, the FBA method detects subtle modulations in the amplitude and frequency of the waveform but the TDE is comparable for all techniques. When the step change occurring at 0.8 seconds in Fig 7(top) enters the observation window (i.e., the window from 0.12 s to 0.8 s) the amplitude step is detected by the FBA algorithm and remains in the window for four consecutive iterations until the event is cleared. During this period, the FBA algorithm shows a clear improvement relative to the i-IpDFT technique, while also demonstrating comparable performance to the dynamic phasor method. Furthermore, unlike the CSTFM algorithm, the FBA identifies the dynamics present and estimates the characterizing parameters.

The second case studies a three-phase fault on a 161 kV transmission line caused by a lightning strike [25]. A voltage waveform is adapted from data captured by a Digital Fault Recorder during the event and is analyzed in Fig. 8. It can be observed that the amplitude step at around 0.2 s is identified by the first window containing the step (i.e. the window from 0.14 s to 0.2 s). The step remains in the window for 3 consecutive iterations until it is cleared, around 0.2 s. The TDE comparison shows the improvement in the reconstructed waveform for the FBA technique relative to i-IpDFT algorithm. Furthermore, the FBA performs similarly or better than the dynamic phasor technique, while simultaneously providing insight into the signal dynamic and corresponding parameters. While the gradual

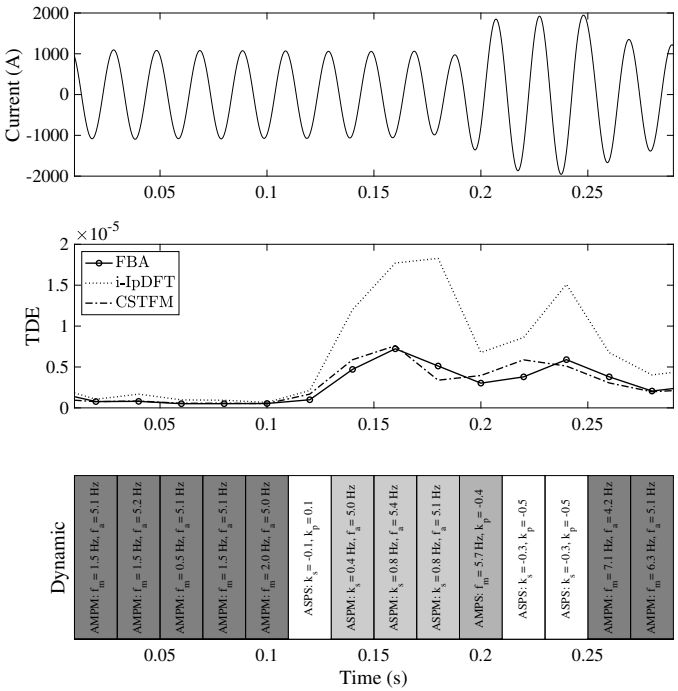

Fig. 7. Analysis of a voltage sag in the MWPI paper manufacturing plant: current waveform adapted from [24] (top), TDE for reconstructed signals using FBA, i-IpDFT and CSTFM algorithms (middle), signal dynamics and parameters estimated by the FBA method (bottom).

amplitude change at 0.3 s can be captured by the dynamic phasor model, the more abrupt amplitude step at 0.2 s is identified and better characterized by the FBA method using the AS dictionary.

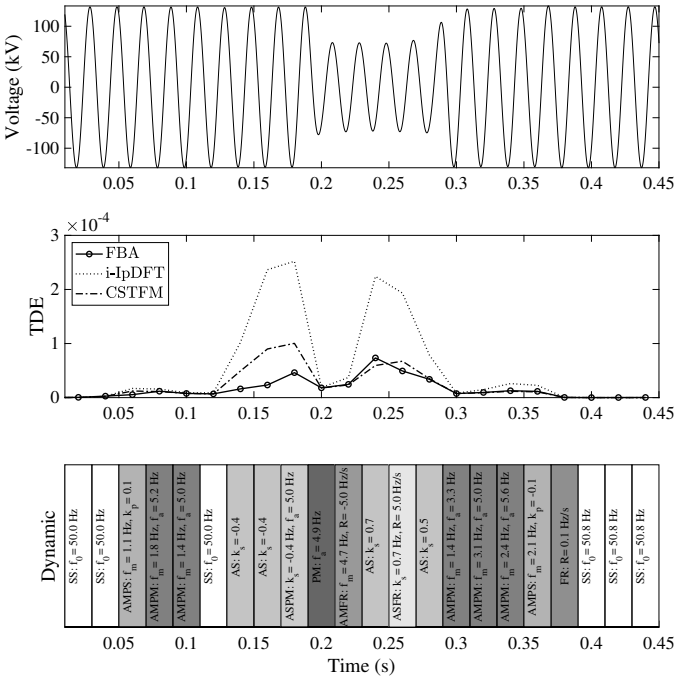

Fig. 8. Analysis of a three-phase fault due to lightning: voltage waveform adapted from [25] (top), TDE for reconstructed signals using FBA, i-IpDFT and CSTFM algorithms (middle), signal dynamics and parameters estimated by the FBA method (bottom).

V. Conclusion

In this paper, we presented a method for detecting and characterizing signal dynamics in power systems. Details on signal dynamic models, dictionary design, signal parameter estimation and dynamic detection were discussed.

For validation, the algorithm was tested on various synthetic and real-world signals and compared to standard and dynamic phasor estimation methods. The results show an improvement in the time and frequency reconstruction with the added benefit of simultaneous signal dynamic identification and parameter estimation. The proposed FBA algorithm is currently capable of identifying amplitude/phase modulations, amplitude/phase steps and frequency ramps as well as steady-state conditions. Further work will involve implementing the algorithm in an FPGA-based device and validating the performance.

While PMUs are limited by steady-state assumptions, forcing operators to interpret phasor estimations during transients, the FBA is not so restricted. The proposed algorithm allows for improved signal and frequency reconstruction and immediate identification of grid dynamics. With further development, we see this method as a flexible and powerful tool for processing power system signals during non-stationary conditions.

Appendix A: Derivation of PDD gradients

The gradient of the objective is adapted from (18) to be:

$$\nabla_\Gamma \Phi = \nabla_\Gamma \mathbf{D}_{Re} \otimes \nabla_{\mathbf{D}_{Re}} \Phi + \nabla_\Gamma \mathbf{D}_{Im} \otimes \nabla_{\mathbf{D}_{Im}} \Phi \tag{24}$$

where $\otimes$ represents the tensor product of two 3-D arrays. This tensor multiplication is defined with the first two indexes used for a simple matrix-matrix product and the third parameter acting as the index of this product [18].

The gradient of each dictionary kernel $\mathbf{d}(\gamma)$ with respect to the parameter set is found easily for each model in Section II-A using (10) and (11) and the following relationship:

$$\frac{\partial \mathbf{d}(k)}{\partial \gamma} = \frac{\partial}{\partial \gamma} \sum_{l=0}^{L-1} W_L^{kl} x_l(\gamma) = \sum_{l=0}^{L-1} W_L^{kl} \frac{\partial x_l(\gamma)}{\partial \gamma} \tag{25}$$

The partial derivative of the objective with respect to the real and imaginary components of the dictionary is shown in (26) and (27):

$$\begin{aligned}\nabla_{\mathbf{D}_{Re}} \Phi = {} & 4\mathbf{D}_{Re}\mathbf{D}'_{Re}\mathbf{D}_{Re} + 4\mathbf{D}_{Re}\mathbf{D}'_{Im}\mathbf{D}_{Im} - 4\mathbf{D}_{Re}\mathbf{G}_{Re} \\ & + 4\mathbf{D}_{Im}\mathbf{D}'_{Im}\mathbf{D}_{Re} - 4\mathbf{D}_{Im}\mathbf{D}'_{Re}\mathbf{D}_{Im} - 4\mathbf{D}_{Im}\mathbf{G}_{Im}.\end{aligned} \tag{26}$$

$$\begin{aligned}\nabla_{\mathbf{D}_{Im}} \Phi = {} & 4\mathbf{D}_{Im}\mathbf{D}'_{Re}\mathbf{D}_{Re} + 4\mathbf{D}_{Im}\mathbf{D}'_{Im}\mathbf{D}_{Im} - 4\mathbf{D}_{Im}\mathbf{G}_{Re} \\ & + 4\mathbf{D}_{Re}\mathbf{D}'_{Re}\mathbf{D}_{Im} - 4\mathbf{D}_{Re}\mathbf{D}'_{Im}\mathbf{D}_{Re} - 4\mathbf{D}_{Re}\mathbf{G}_{Im}.\end{aligned} \tag{27}$$

Appendix B: Derivation of FBA gradients

Let the kernel and signal be represented as $\mathbf{d}(\gamma) = \mathbf{d}_{Re}(\gamma) + j\mathbf{d}_{Im}(\gamma)$ and $X = X_{Re} + jX_{Im}$. Then, analogous to the PDD method, the gradient of the objective with respect to the parameters γ can be expressed as:

$$\frac{\partial \Phi(\gamma)}{\partial \gamma} = \frac{1}{2\sqrt{\Psi(\gamma)}} \left[\frac{\partial \mathbf{d}_{Re}}{\partial \gamma} \frac{\partial \Psi(\gamma)}{\partial \mathbf{d}_{Re}} + \frac{\partial \mathbf{d}_{Im}}{\partial \gamma} \frac{\partial \Psi(\gamma)}{\partial \mathbf{d}_{Im}} \right]. \tag{28}$$

Let $c_1 = X'_{Re}\mathbf{d}_{Re}$, $c_2 = X'_{Im}\mathbf{d}_{Re}$, $c_3 = X'_{Re}\mathbf{d}_{Im}$, $c_4 = X'_{Im}\mathbf{d}_{Im}$, $c_5 = \mathbf{d}'_{Re}\mathbf{d}_{Re}$, $c_6 = \mathbf{d}'_{Im}\mathbf{d}_{Im}$ and $b = (c_1^2 + c_2^2 + c_3^2 + c_4^2 + 2c_1c_4 - 2c_2c_3)$. After some manipulations, the gradients $\frac{\partial \Psi}{\partial \mathbf{d}_{Re}}$ and $\frac{\partial \Psi}{\partial \mathbf{d}_{Im}}$ can be expressed as (29) and (30).

$$\begin{aligned}\frac{\partial \Psi}{\partial \mathbf{d}_{Re}} = {} & 2b\mathbf{d}_{Re} + (c_5 + c_6 - 2)(2c_1X_{Re} + ... \\ & 2c_2X_{Im} + 2c_4X_{Re} - 2c_3X_{Im}).\end{aligned} \tag{29}$$

$$\begin{aligned}\frac{\partial \Psi}{\partial \mathbf{d}_{Im}} = {} & 2b\mathbf{d}_{Im} + (c_5 + c_6 - 2)(2c_3X_{Re} + ... \\ & 2c_4X_{Im} + 2c_1X_{Im} - 2c_3X_{Re})\end{aligned} \tag{30}$$

Appendix C: Harmonic detection

In order to estimate harmonic tones, Algorithm 3 is first used to approximate the fundamental frequency, which should be only minorly affected by the harmonic components given the frequency range under analysis (20-80 Hz) and assuming there are no inter-harmonics close to the fundamental. Once the fundamental is approximated, the frequencies of the harmonics are locked in at integer multiples of this fundamental, so only the amplitude and phase of these components is unknown. A baseline signal $\hat{x}(t) = \hat{x}_0(t) + \hat{x}_1(t) + ... + \hat{x}_H(t)$ and its frequency spectrum $\hat{X}$ can be constructed with the estimated fundamental and a finite number of harmonics present, with an assumed relative amplitude of 0.1 and phase of 0. We can then isolate the frequency bins surrounding each of the located harmonics and project the corresponding segments of the baseline spectrum $\hat{X}$ onto the true spectrum X. The amplitude of the harmonic is then approximated with the magnitude of the projection coefficient:

$$\text{for } h = 1...H \tag{31}$$

$$c_h = \hat{X}_h^* X_h \tag{32}$$

$$\hat{A}_h = |c_h|, \hat{\varphi}_h = \angle c_h \tag{33}$$

For a simple example, we simulate 60 ms of a steady state signal with 80 dB of Gaussian noise, a fundamental frequency of 50.15 Hz and 3rd, 7th and 9th harmonics with relative amplitudes of 5%, 5%, and 1.5%, respectively. The Total Harmonic Distortion (THD) is, therefore, less than 8%. These parameters were selected based on the limits for harmonic voltages specified in the standard EN 50160 [26]. As shown in Fig. 9, the algorithm correctly identifies the fundamental frequency with an error of 1.5 mHz and approximates the relative harmonic amplitudes with errors of 2 to 6% with respect to the reference harmonic amplitudes. The TDE for the reconstructed signal is 2.9E-04 making it comparable to the results for other signal dynamics presented in Table II.

References

[1] AEMO, "Black system South Australia 28 September 2016," 2017.

[2] NERC, "1,200 mw fault induced solar photovoltaic resource interruption disturbance report," NERC, Tech. Rep., 2017.

[3] NERC and WECC, "900 mw fault induced solar photovoltaic resource interruption disturbance report," NERC and WECC, Tech. Rep., 2018.

[4] ENTSO-E, "Oscillation event 03.12.2017," European Network of Transmission System Operators for Electricity, System Protection and Dynamics WG, Tech. Rep., 2018.

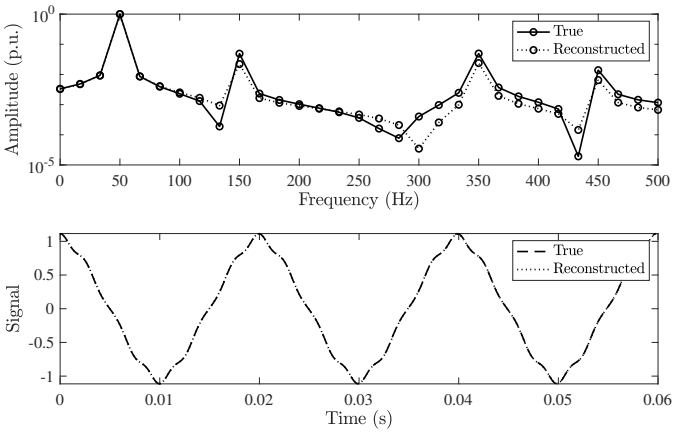

Fig. 9. Frequency spectrum and time-domain waveform of the original and reconstructed signals using an extended version of the FBA algorithm.

[5] J. De La Ree, V. Centeno, J. S. Thorp, and A. G. Phadke, "Synchronized phasor measurement applications in power systems," *IEEE Transactions on Smart Grid*, vol. 1, no. 1, pp. 20–27, 2010.

[6] A.Derviškadić, G.Frigo, M.Paolone, "Beyond Phasors: Modeling of Power System Signals Using the Hilbert Transform," *IEEE Trans. Power Syst.*, 2019.

[7] H. Kirkham and A. Riepnieks, "Dealing with non-stationary signals: Definitions, considerations and practical implications," in *2016 IEEE Power and Energy Society General Meeting (PESGM)*, 2016, pp. 1–5.

[8] Martin Vetterli, Jelena Kovačevic, Vivek K Goyal, *Foundations of Signal Processing*. Cambridge University Press, 2014.

[9] M. Paolone, T. Gaunt, X. Guillaud, et al, "Fundamentals of power systems modelling in the presence of converter-interfaced generation," *Electric Power Systems Research*, vol. 189, 2020.

[10] D. Belega, D. Fontanelli, and D. Petri, "Dynamic phasor and frequency measurements by an improved taylor weighted least squares algorithm," *IEEE Trans. on Instr. and Measurement*, vol. 64, no. 8, pp. 2165–2178, 2015.

[11] P. Castello, M. Lixia, C. Muscas, and P. A. Pegoraro, "Adaptive taylor-fourier synchrophasor estimation for fast response to changing conditions," in *2012 IEEE International Instrumentation and Measurement Technology Conference Proceedings*, 2012, pp. 294–299.

[12] M. Bertocco, G. Frigo, C. Narduzzi, C. Muscas, and P. A. Pegoraro, "Compressive sensing of a taylor-fourier multifrequency model for synchrophasor estimation," *IEEE Trans. on Instr. and Meas.*, vol. 64, no. 12, pp. 3274–3283, 2015.

[13] J. A. de la O Serna, "Analyzing Power Oscillating Signals With the O-Splines of the Discrete Taylor–Fourier Transform," *IEEE Trans. Power Syst.*, 2018.

[14] L. Chen, W. Zhao, Q. Wang, F. Wang and S. Huang, "Dynamic Harmonic Synchrophasor Estimator Based on Sinc Interpolation Functions," *IEEE Trans. Instr. and Meas.*, 2019.

[15] S. L. Hahn, "Hilbert transforms in signal processing," *Artech House*, 1996.

[16] G. Frigo, D. Colangelo, A. Derviškadić, M. Pignati, C. Narduzzi, and M. Paolone, "Definition of accurate reference synchrophasors for static and dynamic characterization of PMUs," *IEEE Trans. on Instr. and Meas.*, Sept 2017.

[17] Yonina C. Eldar, Gitta Kutyniok, *Compressed Sensing: Theory and Applications*. Cambridge University Press, 2014.

[18] Mehrdad Yaghoobi, Laurent Duadet, Mike E. Davies, "Parametric Dictionary Design for Sparse Coding," *IEEE Trans. on Signal Processing*, vol. 57, no. 12, 2009.

[19] J. A. Tropp, "Complex equiangular tight frames," in *Wavelets XI*, M. Papadakis, A. F. Laine, and M. A. Unser, Eds., vol. 5914, International Society for Optics and Photonics. SPIE, 2005, pp. 1 – 11. [Online]. Available: https://doi.org/10.1117/12.618821

[20] S. Boyd and L. Vandenberghe, *Convex Optimization*. Cambridge University Press, 2004.

[21] K. Duda, "Accurate, guaranteed stable, sliding discrete fourier transform [dsp tips tricks]," *IEEE Signal Processing Magazine*, vol. 27, no. 6, pp. 124–127, 2010.

[22] "IEEE Standard for Synchrophasor Measurements for Power Systems," *IEEE Std C37.118.1-2011 (Revision of IEEE Std C37.118-2005)*, pp. 1–61, Dec 2011.

[23] A. Derviškadić, P. Romano, and M. Paolone, "Iterative-interpolated DFT for synchrophasor estimation: A single algorithm for P- and M-class compliant PMUs," *IEEE Trans. on Instr. and Meas.*, vol. 67, no. 3, pp. 547–558, Mar. 2018.

[24] M. Radmehr, S. Farhangi, and A. Nasiri, "The power of paper - effects of power quality distortions on electrical drives and trasformer life in paper industries," *IEEE Industry Applications Magazine*, vol. 13, no. 5, pp. 38–48, 2007.

[25] S. Das, S. Navalpakkam Ananthan, and S. Santoso, "Relay performance verification using fault event records," *Protection and Control of Modern Power Systems*, vol. 3, 12 2018.

[26] European Committee for Electrotechnical Standardization, "Voltage characteristics of electricity supplied by public electricity networks," 2010.

Alexandra Karpilow was born in Boulder, Colorado, USA, in 1994. She received a B.Sc. in Mechanical Engineering from the University of Colorado Boulder in 2016 and a M.Sc. in Electrical Engineering from the Swiss Federal Institute of Technology of Luasanne (EPFL), Switzerland, in 2019. She is currently pursuing a Ph.D. at EPFL in the Distributed Electrical System Laboratory with a focus on signal analysis of power system measurements.

Asja Derviškadić received the B.Sc. and M.Sc. degrees (Hons.) in electrical engineering from the University of Rome "La Sapienza," Rome, Italy, in 2012 and 2015, respectively, and the Ph.D. degree in electrical engineering from the Swiss Federal Institute of Technology of Lausanne (EPFL), Lausanne, Switzerland, in 2019. In 2019-2020 she was a Postdoctoral researcher at the Distributed Electrical Systems Laboratory (DESL) of EPFL and her research interests focused on synchronized sensing technologies for wide-area situational awareness of electrical grids operating in non-stationary conditions.

Guglielmo Frigo (M'18) was born in Padua, Italy, in 1986. He received the B.Sc. and M.Sc. degrees in biomedical engineering from the University of Padova in 2008 and 2011, respectively, and the Ph.D. degree from the School of Information Engineering in 2015. He served as PostDoc researcher at the Electronic Measurement Research Group, University of Padova (2015-2017), and at the Distributed Electrical Laboratory, Swiss Federal Institute of Technology of Lausanne (2018-2020). In 2020, he was foreign guest researcher at NIST, Gaithersburg, USA. He is currently scientist at METAS, Wabern, Switzerland, where he is responsible for the calibration of PMU and PQ meters. Since 2019, he is Associate Editor of the IEEE Transactions on Instrumentation and Measurement, and member of IEC TC 85. His current research interests include the development of enhanced situational awareness strategies, relying on synchrophasor and sampled value measurements.

Mario Paolone (M'07–SM'10) received the M.Sc. (Hons.) and Ph.D. degrees in electrical engineering from the University of Bologna, Italy, in 1998 and 2002. In 2005, he was an Assistant Professor in power systems with the University of Bologna, where he was with the Power Systems Laboratory until 2011. Since 2011, he has been with the Swiss Federal Institute of Technology, Lausanne, Switzerland, where he is currently Full Professor and the Chair of the Distributed Electrical Systems Laboratory. His research interests focus on power systems with particular reference to real-time monitoring and operational aspects, power system protections, dynamics and transients. Dr. Paolone has authored or co-authored over 300 papers published in mainstream journals and international conferences in the area of energy and power systems that received numerous awards including the IEEE EMC Technical Achievement Award, two IEEE Transactions on EMC best paper awards and the IEEE Power System Dynamic Performance Committee's prize paper award. Dr. Paolone was the founder Editor-in-Chief of the Elsevier journal Sustainable Energy, Grids and Networks.